Ru–B amorphous alloy deposited on mesoporous silica nanospheres: An efficient catalyst for D-glucose hydrogenation to D-sorbitol

Senlin Wang, Wei Wei, Yu Zhao, Hexing Li, Hui Li*

The Education Ministry Key Lab of Resource Chemistry and Shanghai Key Laboratory of Rare Earth Functional Materials, Shanghai Normal University, Shanghai 200234, PR China

ARTICLE INFO

ABSTRACT

In this paper, highly ordered mesoporous silica nanospheres externally covered by methyl groups ($-CH_3$) but internally grafted by aminopropyl groups ($-NH_2$) were used as host matrix for loading Ru–B amorphous alloy nanoparticles (NPs). The $-NH_2$ and the $-CH_3$ groups served synergistically as effective functionalities for highly dispersing Ru–B NPs within the pore channels of the mesoporous host. Such catalyst was used in the liquid-phase D-glucose hydrogenation and delivered much higher activity than industrial Raney Ni and the commercial Ru/C catalysts. Meanwhile, it could be used repetitively for more than 9 times, showing a good potential in practical applications. This work demonstrated that the surface properties of mesoporous materials can be modified through region-selective immobilization of diverse organic groups, which is essential to optimize the catalysis for some reactions.
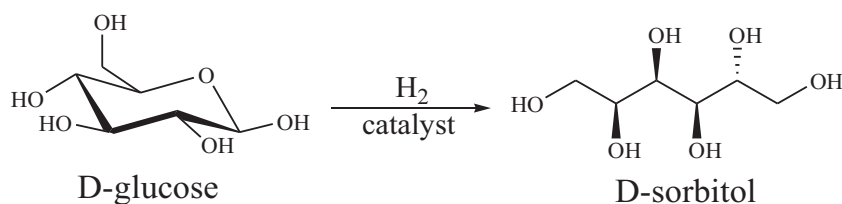
© 2014 Elsevier B.V. All rights reserved.

1. Introduction

As one of the top 12 biobased building blocks listed by the U.S. Department of Energy [1], D-sorbitol is a valuable platform molecule that can be facilely transformed into fuels or chemicals [2,3]. Nowadays, practically all of the D-sorbitol is produced *via* hydrogenation of D-glucose (Scheme 1) [4–11]. Presently, Raney Ni is mainly used in this industrial process [12]. However, the leaching of nickel during hydrogenation and the low activity make this catalyst less profitable, because a refilling of the catalyst and a purification of product to remove residual Ni are necessary, which eventually render this process economically less attractive [13]. Amorphous alloys, a kind of metastable materials with long-range disordered but short-range ordered structure, have attracted growing attention from both academia and industry because of their superior catalytic properties [14,15]. Among them, Ru–B amorphous alloy has proved to be a potential alternative to Raney Ni in hydrogenation of D-glucose to D-sorbitol [16,17]. Although Ru–B amorphous alloy displayed much higher activity during D-glucose hydrogenation to D-sorbitol than Raney Ni, there is still space to enhance the reactivity and stability of the Ru–B nanoparticles (NPs) through depositing them on support by impregnation-reductant method [18]. Because of high surface areas, ordered pore channel,

and uniformity in pore size, highly ordered mesoporous materials can act as promising carriers for depositing M-B (M = transition metal) amorphous alloy NPs [19–21]. Generally, M-B amorphous alloy is prepared by the reduction of metallic ions with borohydride. The reaction is strongly exothermic and releases a huge mass of hydrogen, which put the formed M-B particles out of the pore. As a result, the supported M-B catalysts by using pure mesoporous silica usually exhibit nonuniform distribution of M-B particles and even blockage of the pore entrance, which eventually limits the activity [22,23]. More importantly, the location of M-B on the external surface maybe result in the loss of confinement effect of mesopores on reactivity [23]. In this regard, the design and synthesis of Ru–B NPs located in the ordered pore channels of mesoporous silica represent a promising way to increase the activity and stability.

Presently, mesoporous silica nanospheres (MSNSs) with an average diameter around a few tens of nanometers have been reported [24]. Such silica materials are attractive candidates for catalyst carriers because of their large surface area, short pore channels, as well as regular nanospherical morphologies. Herein, we designed a novel approach to synthesizing highly dispersed Ru–B amorphous alloy catalyst. MCM-41 type MSNSs externally covered by methyl groups ($-CH_3$) but internally grafted by aminopropyl groups ($-NH_2$) were first fabricated. The as-synthesized region-selectively functionalized support was then loaded with uniformly dispersed Ru–B NPs with $-NH_2$ serving as anchor points. This catalyst exhibited high activity during liquid-phase hydrogenation of D-glucose to D-sorbitol. The synergetic promotional

* Corresponding author. Tel.: +86 21 64323578; fax: +86 21 64322272.
    E-mail address: lihui@shnu.edu.cn (H. Li).

Scheme 1. Catalytic hydrogenation of D-glucose to D-sorbitol.

effects from both the —NH$_2$ and the —CH$_3$ surface moieties are well established.

2. Experimental

2.1. Catalyst preparation

All of the chemicals used in this experiment were analytical grade and used without further purification. Raney Ni was commercially available from a D-sorbitol production factory in China and was used without additional activation. Ru/C (5 wt.%) was purchased from Aladdin Industrial Co., Ltd. (Shanghai, China).

Pure MCM-41 type MSNSs were synthesized according to the method reported by Gu et al. [24]. In a typical run of synthesis, 0.2 g of cetyltrimethylammonium bromide (CTAB) surfactant was dissolved at 363 K in a solution comprised of 96 mL of water and 0.7 mL of 2 M NaOH, followed by adding 1.0 mL of tetraethoxysilane (TEOS). After being stirred at 363 K for 2 h and aged at 363 K for another 24 h, the solid product was thoroughly washed with water, followed by drying in vacuum at 353 K overnight. The surfactant and other organic residues were extracted by refluxing the sample in ethanol (EtOH) at 353 K for 24 h. The MSNSs sample was finally obtained after being dried at 353 K under vacuum for 8 h.

The synthesis of MCM-41 type MSNSs externally covered by —CH$_3$ groups but internally grafted by —NH$_2$ groups is in two steps. (1) —NH$_2$ group functionalized MSNSs (NH$_2$-MSNSs) were synthesized through CTAB directed co-condensation of TEOS with aminopropyl triethoxysilane (APTES) in an alkaline solution [25]. Briefly, 0.2 g of CTAB was dissolved at 363 K in a solution comprised of 96 mL of water and 0.7 mL of 2 M NaOH, followed by adding 1.0 mL of TEOS and 1.0 mL of APTES. After being stirred at 363 K for 2 h and aged at 363 K for another 24 h, the solid product was thoroughly washed with water, followed by drying in vacuum at 353 K overnight. (2) 1.5 g of the resulting NH$_2$-MSNSs containing the template species were immersed in 50 mL toluene solution containing 1.5 mL methyl triethoxysilane (MTES) and heated under reflux at 343 K for 24 h with N$_2$ protecting [26]. The solid product was thoroughly washed with toluene, refluxed at EtOH solution to remove the surfactant, and dried in vacuum at 353 K for 8 h. The co-functionalized support was denoted as NH$_2$&CH$_3$-MSNSs.

The supported Ru–B amorphous alloy catalysts were synthesized according to the following procedure. 1.0 g of a support was impregnated with a certain mount of RuCl$_3$ aqueous solution overnight. After being dried under microwave irradiation at 393 K for 35 min, 5.0 mL of 2.0 M KBH$_4$ aqueous solution was added dropwise at 273 K and was stirred continuously until no bubbles released. The solid was washed free from Cl$^-$ or K$^+$ ions with deionized water until a pH ∼ 7 was achieved. The as-prepared Ru–B sample was denoted as Ru–B/NH$_2$&CH$_3$-MSNSs. For comparison, the reference Ru–B catalysts were prepared through identical process to that described above for Ru–B/NH$_2$&CH$_3$-MSNSs, except that pure MSNSs and mono-functionalized MSNSs (NH$_2$-MSNSs and CH$_3$-MSNSs) were used as supports, and were denoted as Ru–B/MSNSs, Ru–B/NH$_2$-MSNSs, and Ru–B/CH$_3$-MSNSs.

2.2. Catalyst characterization

The bulk composition and Ru loading were analyzed by means of inductively coupled plasma optical emission spectrometry (ICP-OES; Varian VISTA-MPX). The amorphous structure was determined by X-ray diffraction (XRD; Rigaku D/Max-RB with Cu Kα radiation). The crystallization process was followed by differential scanning calorimetry (DSC; Shimadzu DSC-60) under an N$_2$ atmosphere at the heating rate of 10 K min^{-1}. Solid-state nuclear magnetic resonance (NMR) spectra were collected on a Bruker AV-400 NMR spectrometer. Fourier transform infrared (FTIR) spectra were recorded on a Nicolet Magna 550 spectrometer by KBr technique. Thermogravimetric analysis and differential thermal analysis (TG/DTA) were conducted on a Shimadzu DTG-60 TG/DTA analyzer with a ramping rate of 10 K min^{-1} in 50 mL min^{-1} of air flow. The catalyst shapes and morphologies were observed by both field emission scanning electron microscopy (FESEM; HITACHI S-4800) and transmission electron microscopy (TEM; JEOL JEM2100). The surface electronic states were investigated by X-ray photoelectron spectroscopy (XPS; ULVAC-PHI PHI5000 VersaProbe using Al Kα radiation), during which all Ru–B samples were dried and pretreated *in situ* in pure Ar atmosphere to avoid oxidation. N$_2$ adsorption–desorption isotherms were obtained at 77 K using a Quantachrome NOVA 4000e apparatus. By N$_2$ adsorption, the Brunauer–Emmett–Teller (BET) surface area (S_{BET}) was calculated by using the multiple-point BET method in the relative pressure range of P/P_0 = 0.05–0.2. The active surface area (S_{act}) was measured by the hydrogen chemisorption at room temperature, which was performed on a Micromeritics AutoChem II 2920 instrument using a dynamic pulse method. The sample was purged under an argon flow (purity of 99.997%, treated with an Alltech Oxy-Trap column) at 523 K for 2 h. The pretreated sample was cooled down to room temperature under argon atmosphere, and hydrogen pulses were injected at 303 K until the calculated areas of consecutive pulses were constant. According to the hydrogenation chemisorption, S_{act} of the as-prepared catalyst was calculated assuming Ru/H = 1 and a Ru surface density of 1.64×10^{19} atoms m^{-2} [27]. Every sample was measured for three times. The reproducibility of the results was checked by repeating the measurements for three times on the same catalyst and was found to be within acceptable limits (<±2%).

2.3. Catalytic activity test

The liquid-phase hydrogenation of D-glucose was performed at 3.0 MPa of H$_2$ pressure and 373 K in a 200-mL stainless steel autoclave with a Teflon tube to avoid metal contamination, in which 1.0 g of Ru catalyst and a glucose aqueous solution (50%, w/w in 50 mL H$_2$O) were well mixed. According to the drop of the H$_2$ pressure in the autoclave within 10 min, both the specific activity (the H$_2$ uptake rate per gram of Ru, R_H^m, mmol h^{-1} g$_{Ru}^{-1}$) and the intrinsic activity (the H$_2$ uptake rate per m^2 of Ru, R_H^S, mmol h^{-1} m$_{Ru}^{-2}$) were calculated by using the ideal gas equation. The reaction mixture was sampled at intervals for product analysis through a liquid-phase chromatograph (Agilent 1200) equipped with a
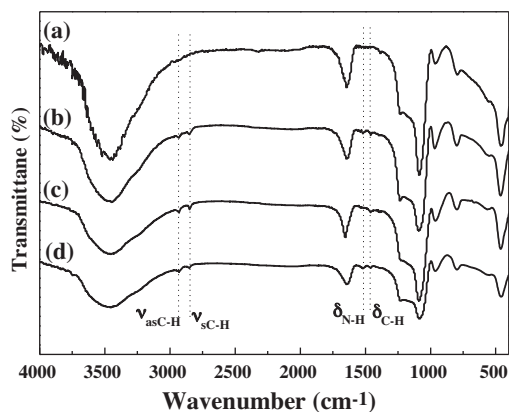
Fig. 1. FTIR spectra of (a) MSNSs, (b) NH_2-MSNSs, (c) CH_3-MSNSs, and (d) NH_2&CH_3-MSNSs.

Fig. 2. ^{29}Si MAS NMR spectra of (a) MSNSs, (b) NH_2-MSNSs, (c) CH_3-MSNSs, and (d) NH_2&CH_3-MSNSs.

carbohydrate column (Shodex, SC1011) and a refractive index detector at 333 K with water as movable phase at 0.50 mL min^{-1}. All the supports alone did not show any catalytic activity. Preliminary kinetic studies revealed that there was a plateau in the dependency of the reaction initial rate upon the stirring rate above 1000 rpm and that the reaction initial rate varied linearly with catalyst amount from 0.1 to 2.0 g, indicating that the stirring rate of 1200 rpm was high enough that the hydrogenation rates were independent of mass transfer. After cooling to room temperature at the end of the reaction, the catalyst was separated by centrifugation and washed with deionized water for further characterizations and applications. In order to determine the catalyst durability, the used Ru–B/NH_2&CH_3-MSNSs catalyst was centrifuged and washed thoroughly with distilled water after each run of the reaction. Then, the Ru–B/NH_2&CH_3-MSNSs was reused with fresh charge of D-glucose for subsequent recycle runs under same reaction conditions. The commercial Ru/C catalyst was reduced in a flow of hydrogen at 423 K for 3 h prior to the reaction.

3. Results and discussion

3.1. Catalyst characterization

The FTIR spectra in Fig. 1 reveal that, besides those absorbance bands observed in the pure mesoporous silica nanospheres (MSNSs), all the functionalized silica (NH_2-MSNSs, CH_3-MSNSs, and NH_2&CH_3-MSNSs) displayed additional absorbance bands at 2930, 2849 and 1460 cm^{-1}, corresponding to the asymmetric stretching, symmetric stretching and bending vibrations of aliphatic C—H
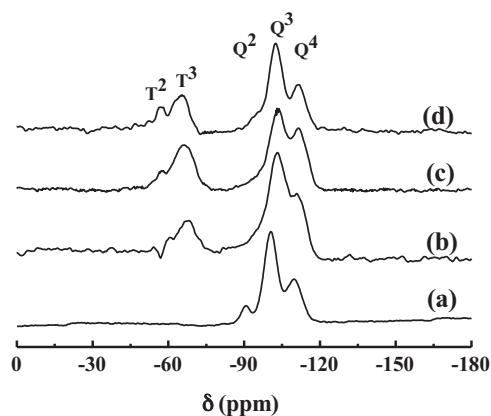
bonds [28]. Additionally, both the NH_2-MSNSs and the NH_2&CH_3-MSNSs displayed absorbance band at 1519 cm^{-1} characteristic of N—H bending vibration. These results demonstrated the successful incorporation of aminopropyl and methyl groups into the silica network, which could be further confirmed by the solid-state NMR spectra. As shown in Fig. 2, the ^{29}Si CP MAS NMR spectra of all the as-made carriers displayed three up-field resonance peaks for the siloxane corresponding to Q^4 ($\delta = -111$ ppm), Q^3 ($\delta = -103$ ppm) and Q^2 ($\delta = -93$ ppm), where $Q^n = Si(OSi)_n(OH)_{4-n}$ ($n = 2-4$). For all the functionalized silica (Fig. 2b–d), two down-field organosilane signals were observed at -66 and -55 ppm, corresponding to T^3 and T^2, where $T^m = RSi(OSi)_m(OH)_{3-m}$ ($m = 1-3$), which demonstrated the incorporation of the organic groups into the silica framework via forming C—Si bond [29]. Additionally, the TGA/DTA curves (Fig. 3) revealed that, besides the weight loss before 423 K due to the desorption of physically adsorbed solvents, all the functionalized carriers displayed weight loss between 463 and 873 K, corresponding to the oxidation removal of the organic groups anchored on MSNSs.

The wide-angle XRD patterns (Fig. 4) demonstrated that, beside a broad peak around $2\theta = 22°$ corresponding to amorphous SiO_2 [30], all the supported Ru–B catalysts displayed only one broad peak around $2\theta = 45°$ indicative of the typical amorphous structure [31]. Fig. 5 shows the XPS spectra of all the supported Ru–B catalysts. Because the core-level at Ru $3d_{3/2}$ is overlapped with that of C $1s$ [32], the core-level at the Ru $3d_{5/2}$ peak was chosen to determine the electronic state of Ru species. Only one peak around a binding energy (BE) at ca. 280.0 eV was observed in the Ru $3d_{5/2}$ level, indicating that almost all of the Ru species were present as
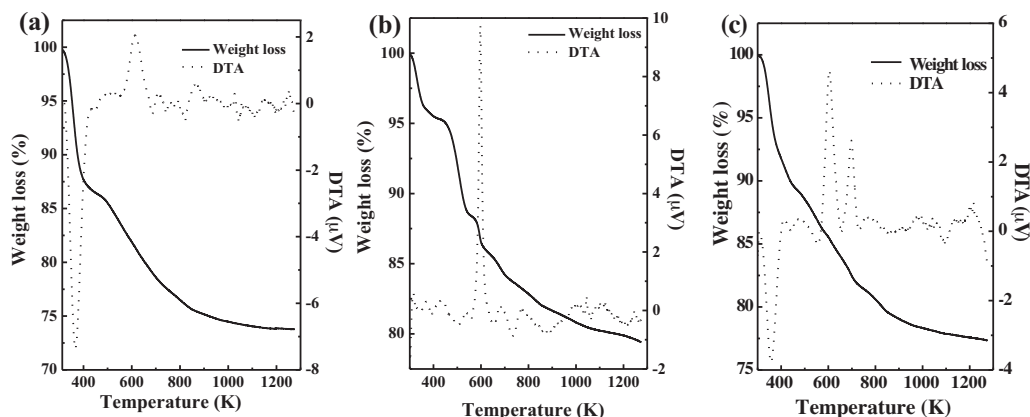

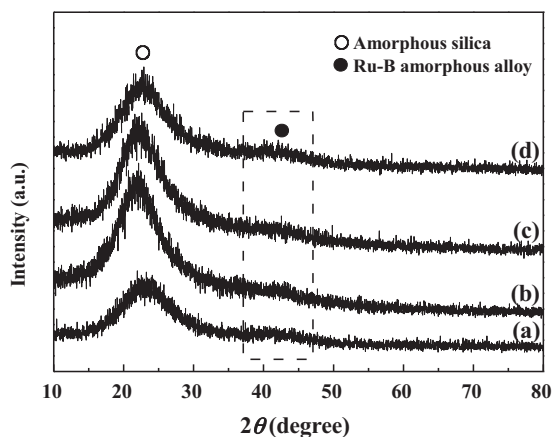**Fig. 3.** TGA and DTA curves of (a) NH_2-MSNSs, (b) CH_3-MSNSs, and (c) NH_2&CH_3-MSNSs.

Fig. 4. Wide-angle XRD patterns of (a) Ru–B/MSNSs, (b) Ru–B/NH$_2$-MSNSs, (c) Ru–B/CH$_3$-MSNSs, and (d) Ru–B/NH$_2$&CH$_3$-MSNSs.
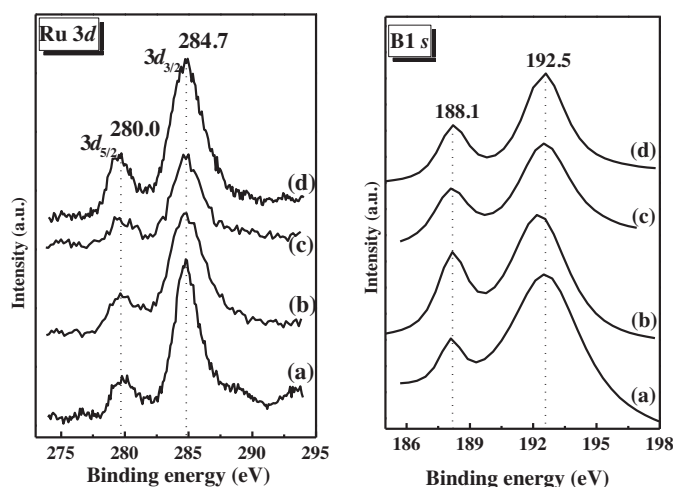

Fig. 5. XPS of (a) Ru–B/MSNSs, (b) Ru–B/NH$_2$-MSNSs, (c) Ru–B/CH$_3$-MSNSs, and (d) Ru–B/NH$_2$&CH$_3$-MSNSs.

metallic state in all the supported catalysts [33]. But the B species were present in both the elemental B and the oxidized B, with B 1s BE values of around 188.1 and 192.5 eV in B 1s level. The B 1s BE of the elemental B in all the supported catalysts exceeded that of pure B (187.1 eV) [34] by 1.0 eV, further indicating that the elemental B is alloyed with the metallic Ru. In alloys, partial electrons may be transferred from B to Ru, as has been detected in the unsupported Ru–B amorphous alloy [16]. The failure in observing the BE shift of the metallic Ru can be understood by considering its relatively greater atomic weight compared with the B atom [34]. The combined results from both the XPS and the aforementioned XRD demonstrated that all the supported Ru–B catalysts were present in the Ru–B amorphous alloy.

As shown in FESEM image (Fig. 6a), the as-prepared MSNSs are present in the form of uniform spheres with an average diameter around 90 nm, which is similar to the previous report [24]. FESEM images of both the NH$_2$&CH$_3$-MSNSs (Fig. 6b) and the Ru–B/NH$_2$&CH$_3$-MSNSs (Fig. 6c) also display similar spherical morphology to the pure MSNSs, demonstrating that the resulting organo-inorganic material (NH$_2$&CH$_3$-MSNSs) preserves the characteristic spherical morphology of MSNSs and deposition of Ru–B did not change the morphology of the parent support. The Ru loadings on the support and the bulk compositions of the Ru–B amorphous alloys were determined by ICP-OES analysis. As shown in Table 1, all the supported catalysts possessed
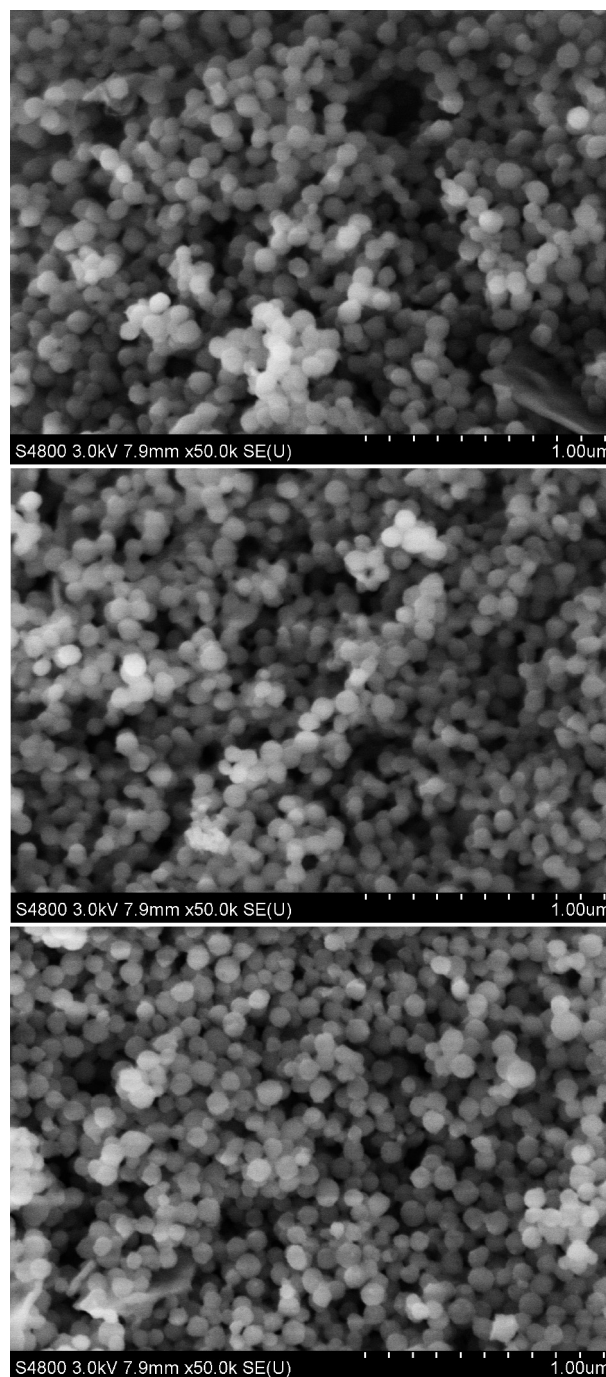

Fig. 6. FESEM images of (a) MSNSs, (b) NH$_2$&CH$_3$-MSNSs, and (c) Ru–B/NH$_2$&CH$_3$-MSNSs.

similar Ru loading and bulk composition regardless of the surface functionalities, indicating that the functionalizing on the surface of carrier with organic groups had no significant influence on the nature of the Ru–B amorphous alloys. However, the S_{act} in Table 2 demonstrated that, with the similar Ru loadings, the surface property of support had remarkable impact on the dispersion degree of the Ru active sites. The S_{act} values changed in the following sequence: Ru–B/MSNSs < Ru–B/NH$_2$-MSNSs ≈ Ru–B/CH$_3$-MSNSs < Ru–B/NH$_2$&CH$_3$-MSNSs, which is mainly attributed to the difference in the location of Ru–B particles.

To investigate the location of Ru–B on the different carriers, all the supported Ru–B catalysts were subject to TEM analysis (Fig. 7). The TEM images further confirmed that all the as-made

Table 1
Textural properties of the as-prepared samples.

Sample	Composition (at.%)	Ru loading (wt.%)	S_{BET} ($m^2\,g^{-1}$)	D_p (nm)	V_p ($cm^3\,g^{-1}$)
MSNSs	/	/	914	3.2	1.31
Ru–B/MSNSs	$Ru_{87}B_{13}$	4.2	377	1.9	0.56
NH$_2$-MSNSs	/	/	868	2.8	0.90
Ru–B/NH$_2$-MSNSs	$Ru_{88}B_{12}$	4.1	382	1.9	0.43
CH$_3$-MSNSs	/	/	898	2.9	0.85
Ru–B/CH$_3$-MSNSs	$Ru_{89}B_{11}$	4.3	355	1.7	0.49
NH$_2$&CH$_3$-MSNSs	/	/	838	2.9	0.88
Ru–B/NH$_2$&CH$_3$-MSNSs	$Ru_{89}B_{11}$	4.4	685	2.6	0.67

Table 2
Structural characteristics and catalytic properties of the as-prepared catalysts.[a]

Catalyst	S_{act} ($m^2\,g^{-1}$)	R_H^m ($mmol\,h^{-1}\,g_M^{-1}$)	R_S^m ($mmol\,h^{-1}\,m_M^{-2}$)	Conversion (%)
Ru–B/MSNSs	18	182.0	93	67
Ru–B/NH$_2$-MSNSs	22	2270	103	88
Ru–B/CH$_3$-MSNSs	21	2215	105	86
Ru–B/NH$_2$&CH$_3$-MSNSs	25	3325	133	99
Raney Ni[b]	45	4.791	0.11	4.5
Ru/C[c]	7.5	580.7	77	23
Crystallized Ru–B/NH$_2$&CH$_3$-MSNSs[d]	10	716.4	72	22

[a] Reaction conditions: 1.0 g catalyst, D-glucose aqueous solution (50 wt.%, 50 mL), T = 373 K, p_{H_2} = 3.0 MPa, reaction time = 80 min, stirring rate = 1200 rpm.
[b] 1.0 g Raney Ni was used.
[c] 0.8 g 5 wt.% Ru/C was used.
[d] Obtained by treating the Ru–B/NH$_2$&CH$_3$-MSNSs at 873 K under N$_2$ flow for 2 h.

carriers were present in the form of uniform nanospheres, in agreement with the above FETEM characterizations. Meanwhile, the TEM images demonstrated that these nanospheres contained highly ordered mesoporous channels similar to MCM-41 [35], which can be well maintained after depositing Ru–B NPs. Different location of Ru–B over all the supports could be also observed clearly from TEM images. In the Ru–B/MSNSs catalyst (Fig. 7b), Ru–B nanowires within the channels of MSNSs can be observed clearly. This can be due to the agglomeration of the produced Ru–B NPs located inside the pore channels together to form nanowires during the preparation process [36]. Furthermore, a portion of Ru–B NPs situated on the external surface of MSNSs can be also observed, because some particles were larger than the pore size of MSNSs. The formation of big Ru–B NPs located on the external surface of MSNSs can be attributed to the inherent limitation of the present catalyst preparation method [19]. During the preparation process, the deposition of Ru–B occurred in the channels accompanied by the release of a huge mass of hydrogen which pushed the formed Ru–B particles out of the channels and aggregated on the external surface of MSNSs [19]. Perhaps, the liberated hydrogen changed the surface energy or properties of the mesopore walls so that the formed Ru–B particles favorably sought the external surface of MSNSs. For Ru–B/NH$_2$-MSNSs (Fig. 7d), nanowires are absent, which can be attributed to the coordination effect of −NH$_2$ groups originally incorporated in the interior of pores on Ru^{3+} ions. Reduction of these coordinated Ru^{3+} ions with BH$_4^-$ led to the location of Ru–B NPs inside the mesoporous channels [37]. Meanwhile, the relatively smoother reduction between the coordinated Ru^{3+} ions and BH$_4^-$ in comparison with the reduction of free Ru^{3+} ions with BH$_4^-$ might diminish the particle agglomeration taking into account the strong exothermicity of such reduction reaction [37]. However, some big NPs can be still observed on the external surface. To inhibit Ru–B NPs from locating on the external surface of MSNSs, we functionalized the external surface of silica with −CH$_3$ groups. Indeed, big NPs located on the external surface are avoided for Ru–B/CH$_3$-MSNSs (Fig. 7f), due to the high hydrophobic external surface. However, Ru–B nanowires appear as dark rod-like objects between the walls of MSNSs, which can be due to the absence of stabilizing groups inside the pore channels. Moreover, Ru–B NPs-aggregates can be observed in Ru–B/CH$_3$-MSNSs (marked with arrow). This is due

to the fall of Ru–B NPs from the pore channels of support. For Ru–B/NH$_2$&CH$_3$-MSNSs (Fig. 7h), no aggregated Ru–B NPs were observed, which is apparently due to both the stabilizing effect of −NH$_2$ groups on Ru^{3+} ions and the high hydrophobic external surface deriving from −CH$_3$ groups.

The low-angle XRD patterns (Fig. 8) reveals that all the carriers displayed well-resolved Bragg diffraction peaks, indexed as (1 0 0), (1 1 0), and (2 0 0) reflections, which are characteristic of a two-dimensional hexagonal ($p6mm$) structure [35]. These sharp diffraction peaks suggest the presence of highly long-range ordered structure of the as-prepared nanocarriers. Deposition with Ru–B caused significant decrease in the intensity of the (1 0 0) diffraction peaks and even the disappearance of the (1 1 0) and (2 0 0) diffraction peaks, implying the reduced ordering degree of the mesoporous structure that could be mainly attributed to the occupation of Ru–B in the pore channels. Moreover, depositing Ru–B resulted in marked shift of the (1 0 0) diffraction peak toward the higher angle region, suggesting a shrinkage of the cell dimension as a result of Ru–B loading. It is to be noted that depositing similar amount of Ru on the NH$_2$&CH$_3$-MSNSs caused the most slight decrease in the intensity of (1 0 0) diffraction peak (Fig. 8d). This further suggests the highest dispersion of Ru–B NPs on the bi-functionalized support as confirmed by both the TEM and the hydrogen chemsorption experiments.

Fig. 9 shows N$_2$ adsorption–desorption isotherms for all the synthesized samples. The characteristic type IV BET isotherms for the as-made nanocarriers show the presence of cylindrical mesoscale pores. The sharp N$_2$ condensation steps at p/p_0 = 0.25–0.4 indicate that all the supports have a highly ordered pore system, in agreement with the findings reported previously [24]. Based on the desorption branches of N$_2$ sorption isotherms, some structural parameters were calculated and listed in Table 1. It can be found that the incorporation of the organic groups into MSNSs caused significant decrease in the S_{BET}, average pore size (D_p) and pore volume (V_p), which could be due to the coverage of the wall surface with these organic functionalities. Upon Ru–B loading, marked decrease in S_{BET}, D_p and V_p values was noted for Ru–B/MSNSs, Ru–B/NH$_2$-MSNSs, and Ru–B/CH$_3$-MSNSs, which was attributed to the blockage of pore channels by the formed Ru–B; however, slighter reduction in these values was observed for
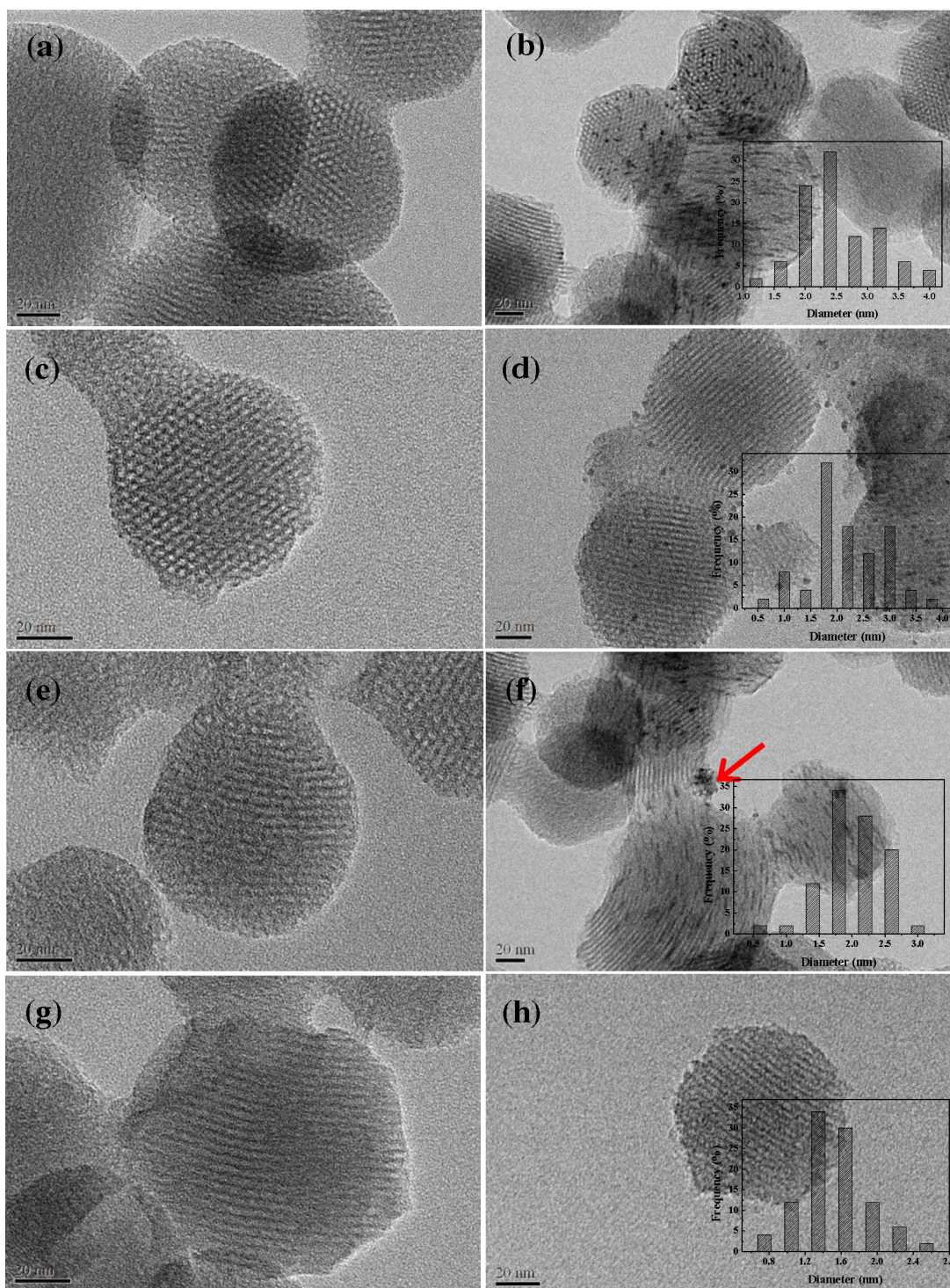
Fig. 7. TEM images of (a) MSNSs, (b) Ru–B/MSNSs, (c) NH₂-MSNSs, (d) Ru–B/NH₂-MSNSs, (e) CH₃-MSNSs, (f) Ru–B/CH₃-MSNSs, (g) NH₂&CH₃-MSNSs, and (h) Ru–B/NH₂&CH₃-MSNSs. The insets are the corresponding Ru–B size distribution histograms.

Ru–B/NH₂&CH₃-MSNSs, suggesting that Ru–B NPs dispersed well on the bi-functionalized MSNSs.

The DSC curves of all the supported Ru–B samples (Fig. 10) further confirmed the amorphous structure of Ru–B, because exothermic peaks can be observed for all the catalysts. Apparently, the enhanced thermal stability could be achieved through functionalizing the frameworks of silica carrier. This is firstly related to the stabilizing effect of —NH₂ groups. On the other hand, the location of the uniform Ru–B NPs in the channel of carrier may inhibit the

particle migration and agglomeration, a key step in the crystallization process [38].

3.2. Catalysis performances

During the liquid-phase hydrogenation of D-glucose, all the Ru-based catalysts displayed 100% selectivity toward D-sorbitol. As shown in Fig. 11a, the change of initial reaction rate ($R_H{}^m$) with D-glucose concentration demonstrates that the hydrogenation of
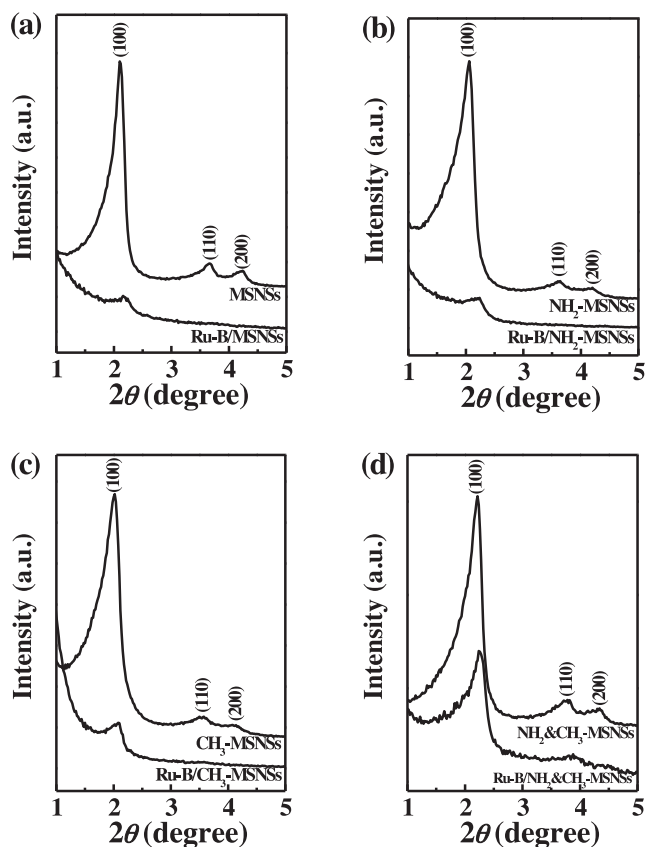
Fig. 8. Low-angle XRD patterns of (a) MSNSs and Ru–B/MSNSs, (b) NH$_2$-MSNSs and Ru–B/NH$_2$-MSNSs, (c) CH$_3$-MSNSs and Ru–B/CH$_3$-MSNSs, and (d) NH$_2$&CH$_3$-MSNSs and Ru–B/NH$_2$&CH$_3$-MSNSs.

D-glucose on Ru–B/NH$_2$&CH$_3$-MSNSs catalyst followed the classic Langmuir-Hinshelwood model as observed by Crezee et al. [39]. At low D-glucose concentration the reaction showed an apparent first order dependency, while at high concentration this changed to zero order behavior. Meanwhile, $R_H{}^m$ increased almost linearly with an increase in hydrogen pressure (Fig. 11b), implying the first-order kinetics with respect to hydrogen. The kinetic behaviors in Fig. 11 could be understood by considering the difference in the adsorption strength between D-glucose and hydrogen on the Ru–B amorphous alloys. Due to its stronger adsorption, D-glucose can reach to saturated adsorption rapidly even at low concentration. Accordingly, the change in the D-glucose concentration has no influence on either the adsorption amount of D-glucose on the catalyst or the hydrogenation rate. At low D-glucose concentration, the hydrogenation rate increased with the enhancement of D-glucose concentration as its surface adsorption was unsaturated. However, the adsorption for hydrogen on Ru–B is relatively weak and cannot reach surface saturation under the present conditions. As a result, the D-glucose hydrogenation exhibited a first order dependency with respect to hydrogen in the operating regime studied.

Table 2 summarized some of the catalytic parameters over the different catalysts during liquid-phase D-glucose hydrogenation. Although Raney Ni possessed a much higher S_{act} than all the Ru-based catalysts, it still exhibited a much lower $R_H{}^m$ and D-glucose conversion within 80 min because of its extremely lower intrinsic activity ($R_H{}^S$). This suggests that Ru was much more active than Ni in nature for D-glucose hydrogenation [40,41]. On the basis of the dependence of the logarithm of $R_H{}^m$ on the reciprocal of the reaction temperature (Fig. 12), the apparent activation energy (E_a)

of D-glucose hydrogenation on the Ru–B/NH$_2$&CH$_3$-MSNSs catalyst was determined to be 19.4 kJ mol^{-1}, much lower than that obtained over Raney Ni (52.8 kJ mol^{-1}), further confirming that the Ru active sites in the former were more active than those in the latter. The enhanced intrinsic activity of Ru had been also demonstrated by comparing the activities of Ru- and Ni-based catalysts during the D-glucose hydrogenation in other groups [9,40].

Even if D-glucose hydrogenation was performed under a lower hydrogen pressure, Ru–B/NH$_2$&CH$_3$-MSNSs delivered far better initial specific activity (3.3 mol h^{-1} g$_{Ru}{}^{-1}$ at 373 K under 3 MPa of hydrogen) than that over the Ru/C (1.1 mol h^{-1} g$_{Ru}{}^{-1}$ at 373 K under 8 MPa of hydrogen) reported by Gallezot et al. [42]. For comparison, a commercial Ru/C catalyst (5 wt.% Ru loading) was measured under the same reaction conditions, and only 23% conversion of D-glucose was achieved using Ru/C within 80 min (Table 2). Apparently, the superior activities of the as-prepared Ru–B amorphous alloys to the commercial Ru/C can be attributed to both the higher S_{act} and the enhanced intrinsic activity. The superior $R_H{}^S$ of the as-prepared Ru–B catalysts could be linked to their unique amorphous alloy structure, which had proven to be favorable for hydrogenation processes [15]. This could be also supported by the fact that an abrupt decrease in activity was observed for the Ru–B/NH$_2$&CH$_3$-MSNSs treated at 873 K for 2 h in N$_2$ flow (Table 2), which was firstly due to the significant agglomeration of Ru–B NPs at elevated temperatures and, thus, decreasing S_{act} and, secondly, the decrease in $R_H{}^S$ resulted from the crystallization of Ru–B amorphous alloy. The larger $R_H{}^S$ of Ru–B/NH$_2$&CH$_3$-MSNSs amorphous alloy catalyst compared to its corresponding crystalline counterpart and the commercial Ru/C can be interpreted in terms of both the structural and the electronic effects: (i) *Structural effect*: the unique short-range ordering but long-range disordering amorphous structure endowed Ru–B amorphous alloy with a stronger synergistic effect between Ru active sites and more highly unsaturated Ru active sites than the crystalline catalyst, which may promote the adsorption of reactants and favor hydrogenation activity [15]. (ii) *Electronic effect:* The aforementioned XPS experiments demonstrated the strong electronic interaction between Ru and B in the Ru–B amorphous alloy, making Ru electron-enriched. The higher electron density on Ru active sites might facilitate the formation of H$^-$ species [41], which could promote D-glucose hydrogenation activity taking into account that the D-glucose hydrogenation was first-order with respect to hydrogen while it was zero-order to the D-glucose. However, no electron donation-acceptance was present in the commercial Ru/C catalyst and the Ru-based crystalline catalyst due to the decomposition of Ru–B during the crystallization process [16,38], which could account for the lower $R_H{}^S$ than the corresponding Ru–B amorphous alloy catalyst.

Based on the $R_H{}^m$ and D-glucose conversion data presented in Table 2, one can see that the reactivity of all the supported Ru–B amorphous alloy catalysts changed in the following sequence: Ru–B/NH$_2$&CH$_3$-MSNSs > Ru–B/NH$_2$-MSNSs ≈ Ru–B/CH$_3$-MSNSs > Ru–B/MSNSs. On one hand, the different hydrogenation activities should be related to the difference in the dispersion degree of Ru active sites (S_{act}) resulted from the diverse promotional effect of surface organic groups, as discussed above. On the other hand, the different activities of all the supported Ru–B catalysts apparently arose from the different intrinsic activity, since the $R_H{}^S$ values changed in a same trend as that of the $R_H{}^m$ and D-glucose conversion. Because the Ru–B deposited on different nanocarriers possessed similar compositions, amorphous alloy structure, as well as surface electronic characteristics, the district location of Ru–B should be considered to be responsible for the diverse $R_H{}^S$. Maybe the pore channels could enrich the D-glucose molecules in the chamber owing to the microreactor effect [43,44]. In addition, the location of Ru–B inside the pore channels can be expected to effectively increase the collision frequency between reactants
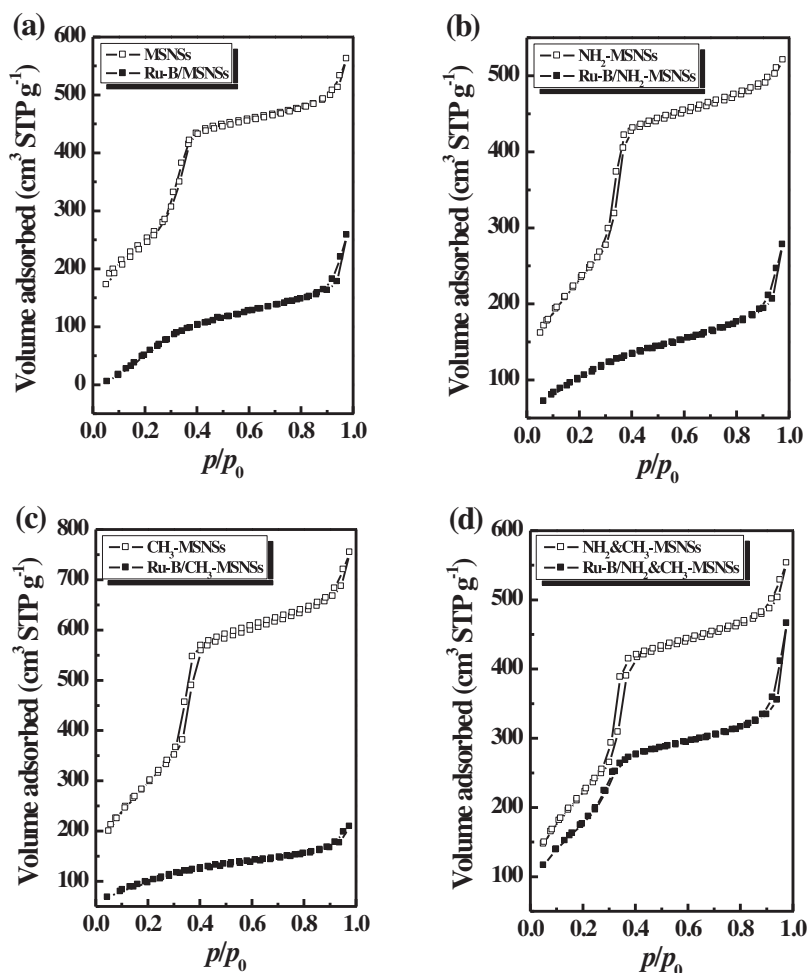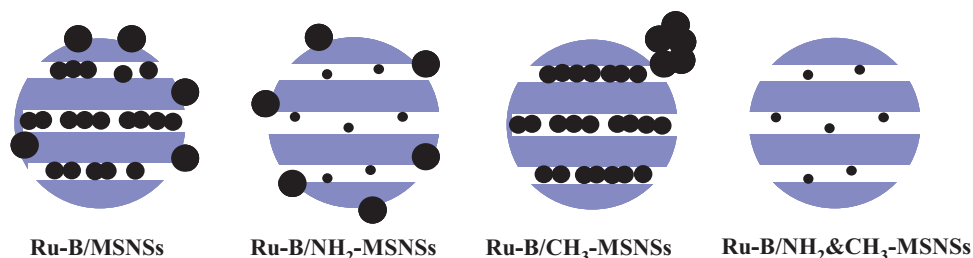
Fig. 9. Nitrogen adsorption–desorption isotherms of (a) MSNSs and Ru–B/MSNSs, (b) NH_2-MSNSs and Ru–B/NH_2-MSNSs, (c) CH_3-MSNSs and Ru–B/CH_3-MSNSs, and (d) NH_2&CH_3-MSNSs and Ru–B/NH_2&CH_3-MSNSs.

and Ru active sites. These factors might possibly account for the different intrinsic activity during D-glucose hydrogenation. Consequently, our results clearly revealed that the region-selective functionalization of the inside and outside surface of carrier was essential for the location of Ru–B particles (Scheme 2) and this could strongly influence the catalytic activity.

The as-prepared Ru–B/NH_2&CH_3-MSNSs catalyst also exhibited strong durability during D-glucose hydrogenation. The recycling test (Fig. 13) shows that Ru–B/NH_2&CH_3-MSNSs can be used repetitively more than 9 times without significant loss of activity. But, after being used repeatedly 10 times, a loss of activity (11%) can be observed for Ru–B/NH_2&CH_3-MSNSs. ICP analysis revealed that no leaching of Ru species could be detected in the reaction mixtures during repetitive runs, implying that this catalyst was stable against

the chelating effect of the reactant and product. To further rule out the leaching of Ru species, the following procedure proposed by Sheldon et al. was carried out [45]. After reaction for 80 min that the D-glucose conversion was 88% on the tenth cycle, the mixture was filtered to remove the solid catalyst and then allowed the mother solution to react for another 1.5 h under the same reaction conditions. No significant change in the conversion of D-glucose was observed, confirming that this reaction really proceeded on the surface of the Ru–B amorphous alloy and the catalysis by the Ru species leached in the solution could be ruled out. TEM image of the used catalyst after 10 cycles (Fig. 14) suggested that the decrease in the activity can be mainly due to the damage of the ordered mesoporous structure of silica, leading to a remarkable agglomeration of Ru–B NPs.

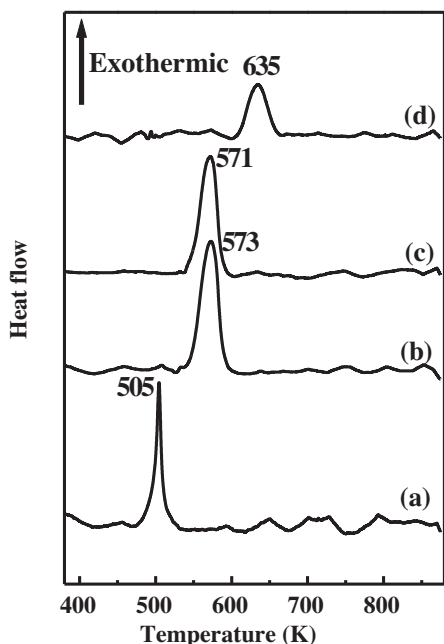**Scheme 2.** Schematic illustration of the location of Ru–B on different carriers.

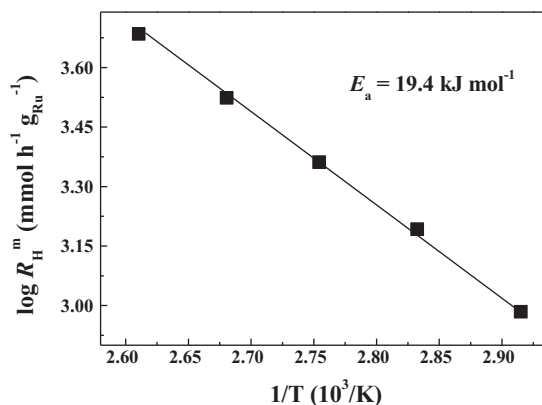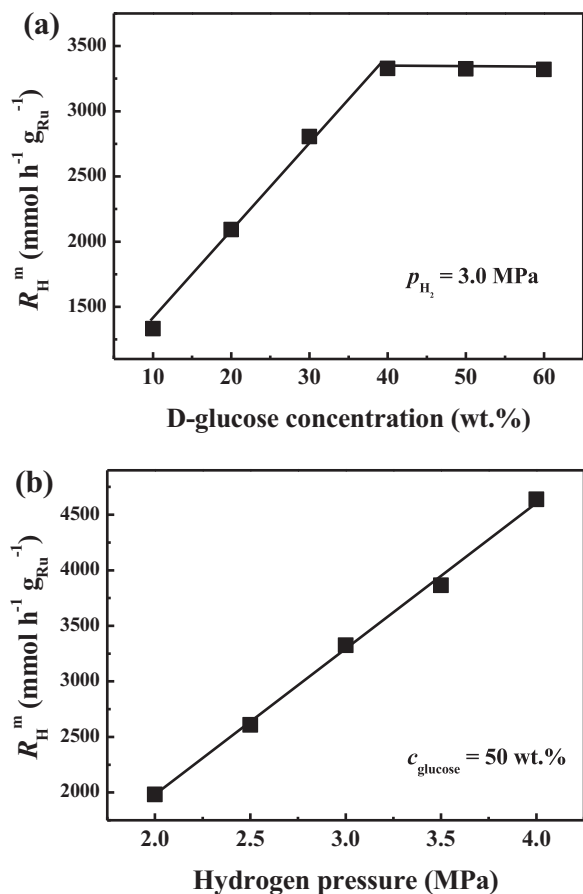**Fig. 10.** DSC curves of (a) Ru–B/MSNSs, (b) Ru–B/NH$_2$-MSNSs, (c) Ru–B/CH$_3$-MSNSs, and (d) Ru–B/NH$_2$&CH$_3$-MSNSs.

Fig. 11. Effect of (a) D-glucose concentration and (b) hydrogen pressure on the initial rate of D-glucose hydrogenation obtained on Ru–B/NH$_2$&CH$_3$-MSNSs. Reaction conditions: 1.0 g of catalyst, T = 373 K, stirring rate = 1200 rpm.
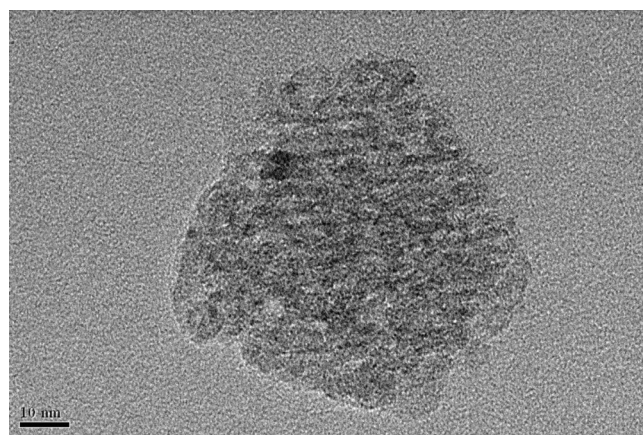

Fig. 12. Arrhenius plot for the D-glucose hydrogenation over Ru–B/NH$_2$&CH$_3$-MSNSs. Reaction conditions are given in Table 2.

Fig. 13. Recycling test of Ru–B/NH$_2$&CH$_3$-MSNSs catalyst for D-glucose hydrogenation. Reaction conditions are given in Table 2.

Fig. 14. TEM image of Ru–B/NH$_2$&CH$_3$-MSNSs after ten consecutive runs for D-glucose hydrogenation. Reaction conditions are given in Table 2.

4. Conclusions

In summary, this work developed a novel mesoporous silica nanospheres externally covered by —CH$_3$ groups but internally grafted by —NH$_2$ groups, which was used as a powerful host for the production of highly dispersed Ru–B amorphous alloy catalyst. The synergetic promoting effects from both the —NH$_2$ and the —CH$_3$ functionalities was considered as one key factor responsible for the location of Ru–B inside the pore channels of the multifunctionalized nanocarrier. During the liquid-phase hydrogenation of D-glucose

to D-sorbitol, the synthesized catalyst exhibited high activity and strong durability owing to the microreactor effect and the confinement effect of the ordered mesoporous structure of support. These results not only greatly extend the application of amorphous alloy but also demonstrate that region-selectively functionalizing the surface of ordered mesoporous materials with diverse groups allows for molecular-level fine-tuning of catalytic performances of the introduced guest materials.

Acknowledgements

References

[1] T. Werpy, G. Peterson, Top Value Added Chemicals from Biomass, vol. 1: Results of Screening for Candidates from Sugars and Synthesis Gas, US Department of Energy, Energy Efficiency and Renewable Energy, Battelle, http://www1.eere.energy.gov/biomass/pdfs/35523.pdf
[2] A. Corma, S. Iborra, A. Velty, Chem. Rev. 107 (2007) 2411.
[3] P.L. Dhepe, F. Fukuoka, Catal. Surv. Asia 11 (2007) 186.
[4] W.S. Fedor, J. Millar, A.J. Accola, Ind. Eng. Chem. 52 (1960) 282.
[5] W.M. Kruse, L.W. Wright, Carbohydr. Res. 64 (1978) 293.
[6] P. Gallezot, P.J. Cerino, B. Blanc, G. Fleche, P. Fuertes, J. Catal. 146 (1994) 93.
[7] S. Kolaric, V. Sunjic, J. Mol. Catal. A 110 (1996) 189.
[8] H. Li, H.X. Li, J.F. Deng, Catal. Today 74 (2002) 53.
[9] B. Kusserow, S. Schimpf, P. Claus, Adv. Synth. Catal. 345 (2003) 289.
[10] S. Schimpf, C. Louis, P. Claus, Appl. Catal. A 356 (2009) 112.
[11] V.N. Sapunov, M.Ye. Grigoryev, E.M. Sulman, M.B. Konyaeva, V.G. Matveeva, J. Phys. Chem. A 117 (2013) 4073.
[12] B.W. Hoffer, E. Crezee, F. Devred, P.R. Mooijman, W.G. Sloof, P.J. Kooyman, A.D. van Langeveld, F. Kapteijn, J.A. Moulijn, Appl. Catal. A 253 (2003) 437.
[13] I. Toufeili, S. Dziedzic, Food Chem. 47 (1993) 17.
[14] Y. Chen, Catal. Today 44 (1998) 3.
[15] Y. Pei, G.B. Zhou, N. Luan, B.N. Zong, M.H. Qiao, F. Tao, Chem. Soc. Rev. 41 (2012) 8140.
[16] H.B. Guo, H.X. Li, J. Zhu, W.H. Ye, M.H. Qiao, W.L. Dai, J. Mol. Catal. A 200 (2003) 213.
[17] H.B. Guo, H.X. Li, Y.P. Xu, M.H. Wang, Mater. Lett. 57 (2002) 392.
[18] J.F. Deng, H.X. Li, W.J. Wang, Catal. Today 51 (1999) 113.
[19] X. Chen, S. Wang, J. Zhuang, M.H. Qiao, K.N. Fan, H.Y. He, J. Catal. 227 (2004) 419.
[20] Y. Wang, L. Xu, L. Xu, H.X. Li, H. Li, Chin. J. Catal. 34 (2013) 1027.
[21] L. Xu, W. Wei, H.X. Li, H. Li, ACS Catal. 4 (2014) 251.
[22] S.T. Wong, J.F. Lee, J.M. Chen, C.Y. Mou, J. Mol. Catal. A 15 (2001) 159.
[23] H. Li, J. Liu, H.X. Yang, H.X. Li, Chin. J. Chem. 27 (2009) 231.
[24] J.L. Gu, W. Fan, A. Shimojima, T. Okubo, Small 3 (2007) 1740.
[25] S.R. Hall, C.E. Fowler, B. Lebeau, S. Mann, Chem. Commun. (1999) 201.
[26] F. de Juan, E. Ruiz-Hitzky, Adv. Mater. 12 (2000) 430.
[27] J.J.F. Scholten, A.P. Pijers, A.M.L. Hustings, Catal. Rev.: Sci. Eng. 27 (1985) 151.
[28] A.S. Maria Chong, X.S. Zhao, J. Phys. Chem. B 107 (2003) 12650.
[29] D.J. Macquarrie, D.B. Jackson, J.E.G. Mdoe, J.H. Clark, N. J. Chem. 23 (1999) 539.
[30] R.M. Rioux, H. Song, J.D. Hoefelmeyer, G.A. Somorjai, J. Phys. Chem. B 109 (2005) 2192.
[31] A. Yokoyama, H. Komiyama, H. Inoue, T. Masumoto, H.M. Kimura, J. Catal. 68 (1981) 355.
[32] R. Schulz, A.V. Neste, P.A. Zielinski, S. Boily, F. Czerwinski, J. Szpunar, S. Kaliaguine, Catal. Lett. 35 (1995) 89.
[33] J.C. Fuggle, T.E. Madey, M. Steinkilberg, D. Menzel, Surf. Sci. 52 (1975) 521.
[34] H. Li, H.X. Li, W.L. Dai, W.J. Wang, Z.G. Fang, J.F. Deng, Appl. Surf. Sci. 152 (1999) 25.
[35] C.T. Kresge, M.E. Leonowicz, W.J. Roth, J.C. Vartuli, J.S. Beck, Nature 359 (1992) 71.
[36] Y.J. Han, J.M. Kim, G.D. Stucky, Chem. Mater. 12 (2000) 2068.
[37] H. Li, Y. Xu, H.X. Yang, F. Zhang, H.X. Li, J. Mol. Catal. A 307 (2009) 105.
[38] H.X. Li, W.J. Wang, H. Li, J.F. Deng, J. Catal. 194 (2000) 21.
[39] E. Crezee, B.W. Hoffer, R.J. Berger, M. Makkee, F. Kapteijn, J.A. Moulijn, Appl. Catal. A 251 (2003) 1.
[40] B.W. Hoffer, E. Crezee, P.R.M. Mooijman, A.D. van Langeveld, F. Kapteijn, J.A. Moulijn, Catal. Today 79–80 (2003) 35.
[41] H. Noller, W.M. Lin, J. Catal. 85 (1984) 25.
[42] P. Gallezot, N. Nicolaus, G. Flèche, P. Fuertes, A. Perrard, J. Catal. 180 (1998) 51.
[43] E.E. Santiso, A.M. George, C. Heath Turner, M.K. Kostov, K.E. Gubbins, M. Buongiorno-Nardelli, M. Sliwinska-Bartkowiak, Appl. Surf. Sci. 252 (2005) 766.
[44] X. Pan, Z. Fan, W. Chen, Y. Ding, H. Luo, X. Bao, Nat. Mater. 6 (2007) 507.
[45] R.A. Sheldon, M.I. Wallau, W.C. Arends, E.U. Schuchardt, Acc. Chem. Res. 31 (1998) 485.